Influence of Land Surface Roughness on Atmospheric Circulation and Precipitation: A Sensitivity Study with a General Circulation Model

Y. C. SUD

Laboratory for Atmospheres, NASA/Goddard Space Flight Center, Greenbelt, Maryland

J. SHUKLA AND Y. MINTZ

Department of Meteorology, University of Maryland, College Park, Maryland

(Manuscript received 23 May 1986, in final form 27 February 1988)

ABSTRACT

The influence of land surface roughness on the large scale atmospheric circulation and rainfall was examined by comparing three sets of simulations made with a general circulation model in which the land surface roughness length, z_0, was reduced from 45 cm to 0.02 cm. The reduced surface roughness produced about a two-fold increase in the boundary layer wind speed and, at the same time, a two-fold decrease in the magnitude of the surface stress. There was almost no change in the surface evaporation and surface sensible heat flux. There was, however, a large change in the horizontal convergence of the water vapor transport in the boundary layer and a corresponding large change in the rainfall distribution mainly as a consequence of the change in the curl of the surface stress. This result suggests that the height of the earth's vegetation cover, which is the main determinant of the land surface roughness, has a large influence on the boundary layer water vapor transport convergence and the rainfall distribution.

1. Introduction

The influence of the land surface boundary conditions on the large scale atmospheric circulation and rainfall has been a matter of speculation for a long time. Only recently have general circulation models been used for the quantitative investigation of this problem. Manabe (1975) and Walker and Rowntree (1977) published the first GCM calculations on the influence of soil moisture and Charney et al. (1977) published the first GCM calculation on the influence of surface albedo. Subsequently, many other soil moisture and surface albedo investigations have been made with GCMs, some of which are described and evaluated in the reviews by Mintz (1984) and by Rowntree (1985). All of those studies showed that soil moisture and albedo have a significant influence on the large scale circulation and rainfall.

More recently, Sud and Smith (1985a) showed that the circulation and rainfall over and adjacent to the Sahara Desert are sensitive to the roughness of the desert surface. In another study, Sud and Smith (1985b) showed that the local surface roughness had a large influence on the summer rainfall over India, and that this influence is as important as that of the surface albedo.

In the present investigation, we examine and interpret the sensitivity of the atmospheric circulation and rainfall to a global change in the land surface roughness. The land surface roughness length, z_0, is changed from 45 cm, which is about the average for all land, to 0.02 cm, a value which is characteristic of a smooth, vegetation free land surface (and is also about the average z_0 for the ocean surface). As in some of the other GCM sensitivity studies, for example the soil moisture sensitivity study of Shukla and Mintz (1982), our goal here is to find the sensitivity of the atmosphere to a very large universal change in one of its boundary conditions.

2. Model description and surface boundary conditions

The general circulation model used for this study has been described by Shukla et al. (1982). The specific version of the model that we use includes all of the modifications indicated by Randall (1982) and by Sud and Smith (1984).

The model uses horizontal spherical coordinates, with a 4° latitude by 5° longitude resolution, and a vertical sigma coordinate system which divides the atmosphere into nine layers of equal mass between the earth's surface and an upper boundary at the pressure of 10 mb. The prognostic physical state atmospheric variables are the pressure at the earth's surface, p_s, the zonal and meridional wind components, u_l and v_l, temperature, T_l, and water vapor mixing ratio, q_l, where l denotes the middle of each of the nine atmo-

Corresponding author address: Dr. Y. C. Sud, Laboratory for Atmospheres, NASA/Goddard Space Flight Center, Greenbelt, MD 20771.

spheric layers, increasing downward. In addition, there are two prognostic land surface temperatures. One is the grid area average ground temperature, T_g, which is used to calculate the upward longwave radiation flux and the sensible heat flux from the land surface to the atmosphere. The other is a simulated moist lysimeter temperature, T_g^*, which is used to calculate the potential evapotranspiration.

The prescribed earth's surface boundary conditions are the July climatological normals. They are the sea surface temperature and sea ice extent from Crutcher and Davis (1969), the surface albedo from Posey and Clapp (1964) as modified by Sud and Fennessy (1982), and the soil wetness from Mintz and Serafini (1984).

In this GCM, the coefficient of the eddy shearing stress between adjacent model layers is of negligible magnitude. Consequently, it is the lowest model layer which acts as the frictionally forced planetary boundary layer.

The calculations of surface stress, surface sensible heat flux and potential evapotranspiration follow Sud and Smith (1984), who re-derived the bulk aerodynamic transfer coefficient from an ensemble averaging approximation of the sub-gridscale variables in the planetary boundary layer following Deardorff (1972). The potential evaportranspiration, E^*, is calculated by assuming that the lysimeter temperature, T_g^*, is in quasi-equilibrium with the PBL temperature and humidity profile above it.

The actual evapotranspiration is $E = \beta E^*$, where β is a function of the prescribed soil wetness, W/W^*, as given by Mintz and Serafini (1984).

The parameterized cumulus convection is an adaptation of Arakawa's (1969, 1972) formulation, which was designed for the UCLA three layer GCM. In that formulation, the moist static energy, $h = c_pT + gz + \lambda q$, and the saturation moist energy, $h^* = c_pT + gz + \lambda q^*$, were defined for each of the three layers where T is the air temperature, q and q^* are the actual and saturation water vapor mixing ratios, z is the geopotential and all quantities are at the center of the sigma-layer. The constants are the specific heat of air at constant pressure, c_p, the latent heat of condensation, λ, and the acceleration due to gravity, g. When this three layer parameterization was put into the nine layer GCM by Somerville et al. (1974), the three degrees of freedom on h and h^* were retained by "strapping" the lowest six model layers into three adjacent pairs with the uppermost three layers excluded from the convection process. (A description of the "strapping" and "unstrapping" procedure can be found in Kalnay et al. 1983, Vol. I, pp. V.49-V.76).

A schematic sketch of the cumulus cloud parameterization scheme is shown in Fig. 1, where the three strapped moist static energies are: $h_L = h_9 + h_8$, $h_M = h_7 + h_6$, and $h_U = h_5 + h_4$. With this scheme, three kinds of cumulus clouds can develop, two of which withdraw water vapor from the lowest strapped layer, L as shown in Fig. 1.

The air within an ascending cloud tower is assumed to be saturated and, therefore, has positive (or negative) buoyancy in the overlying strapped layer, depending on the criterion $h_L > (h_M^*, h_U^*)$ or $(h_L < (h_M^*, h_U^*))$. When $h_U^* > h_L > h_M^*$, shallow nonprecipitating cumulus clouds are produced. When $h_L > (h_M^*, h_U^*)$, deep precipitating cumulus clouds are produced.

The shallow clouds detrain and evaporate the cloud water into the middle strapped layer, as indicated by d_M in Fig. 1. The water vapor added to strapped layer M is removed by one of the other precipitation processes or by horizontal divergence of the water vapor transport. The diverging water vapor must converge

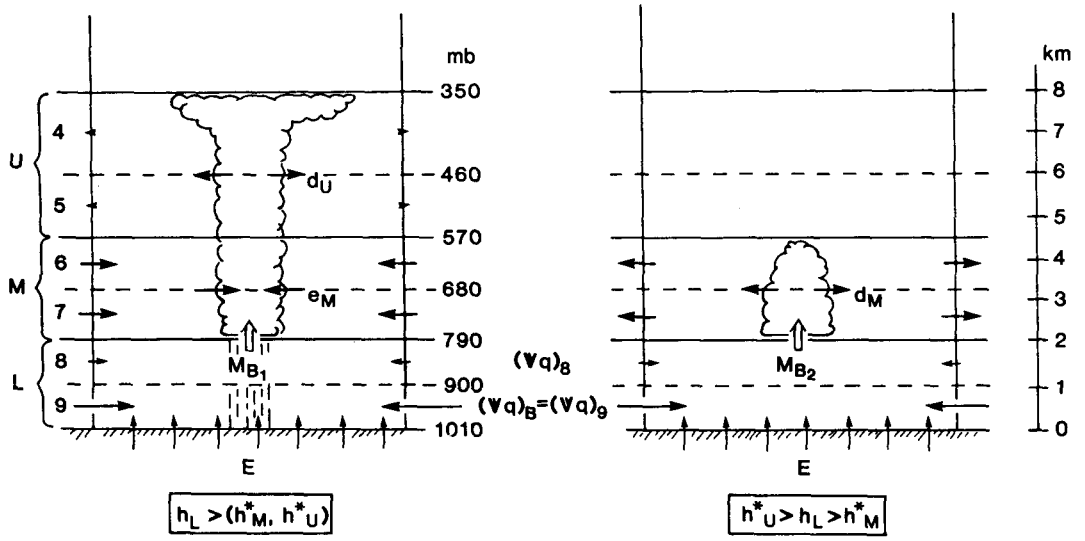

FIG. 1. Strapped-layer cumulus cloud parameterization scheme for shallow and deep cumulus clouds. (For definitions of the symbols, see the text.)

somewhere else. If it converges where there are deep cumulus clouds, it is entrained through the sides of the clouds, as indicated in the figure by e_M, and there it contributes to the convective precipitation. In the upper strapped layer a small amount of cloud water is detrained and evaporates into that layer, as indicated by d_U in the figure. This water vapor is removed by large scale precipitation or is locally removed by horizontal transport divergence and eventually removed from the layer by large scale subsidence. (For the third type of convective cloud, which can produce a small amount of precipitation by withdrawing water vapor from the middle strapped layer, see Kalnay et al. 1983, Vol. I, pp. V.55–V.59).

When the temperature difference between any two adjacent model layers exceeds the dry adiabatic lapse rate, dry convection takes place, which transfers sensible heat from the lower to the higher of the two layers and restores the dry adiabatic lapse rate. In the present version, no vertical transfer of water vapor or momentum is produced by the dry convection. This is a questionable aspect of the dry convection parameterization and we shall refer to it again in section 4.5.

Large scale condensation occurs in any layer when it becomes supersaturated. The raindrops of the large scale condensation evaporate into the unsaturated underlying layers until the layers are saturated. Only the excess water reaches the ground as precipitation.

The large scale condensation clouds are assumed to fill the entire gridbox volume and interact with the short- and longwave radiation fluxes. For the shortwave fluxes, these clouds have a sigma-level dependent prescribed optical thickness. For the longwave fluxes these clouds always have an infinite optical thickness. The convective clouds, on the other hand, are assumed to cover only a small fraction of the grid volume and their influence on both the long and short wave radiation is neglected.

The amount of convective precipitation depends on the local surface evaporation, E, and on the convergence of the horizontal water vapor transport in the lowest strapped layer, $-\nabla_\sigma \cdot [\nabla q \Delta p/g]_L$, because both of these influence q_L and, therefore, influence the convective instability criteria, $h_L \gtrless (h_m^*, h_u^*)$ and $h_m^* < h_L^* < h_u^*$. It is these instability criteria which determine whether the water vapor will be removed by one or more of the following: i) convective clouds; ii) shallow nonprecipitating convective clouds; iii) large scale vertical advection at the top of the layer; or iv) large scale condensation and precipitation from the layer.

3. Experiment design

Three existing simulations for the month of July were used as the control runs. They were also the control runs for the previous study by Sud and Smith (1985b) on the monsoon circulation and rainfall over India. The initial states of the atmosphere for the first two runs were obtained from the National Meteorological Center analyses for 15 June 1979 and 15 June 1980. The third run started on 20 June, using as its initial state the time average of the NMC analyses for the period 7 June through 6 July 1980. In the three control runs, the surface roughness length, z_0, was prescribed as 45 cm everywhere over land. This value was taken from a reference made by Deardorf (1972) to a presentation by Fiedler and Panofsky (1971), in which z_0, was stated to be between 20 and 70 cm ". . . for most land surfaces when averaged over large areas of heterogeneous terrain." In the published account, Fiedler and Panofsky (1972) give z_0 = 42, 99 and 142 cm as the average values for plains, low mountains and high mountains, respectively.

To have a very different land surface roughness length, z_0, in the experiment runs, it was reduced from 45 cm to 0.02 cm everywhere over the land. A change of this magnitude produces about a four to five-fold reduction in the bulk aerodynamic surface drag coefficient, $C_D \equiv C_U^2$, with a planetary boundary layer that is about 1 km deep (cf. Sud and Smith 1984, Fig. 1a). The actual variation of z_0 between a tropical rain forest ($z_0 \approx 200$ cm) and a desert ($z_0 \approx 1$ cm) (see Baumgartner et al. 1977, Figs. 1 and 2), also produces about a four-fold reduction in the bulk aerodynamic drag coefficient, with a one km deep boundary layer. Moreover, because z_0 = 0.02 cm is taken as the surface roughness length of the oceans in all the runs, the experiments can be interpreted as studying the effect of making the land surface as smooth as the oceans, but with actual orography.

In all of our analyses (except Fig. 12), we compare the ensemble mean of the three Julys for the control with the ensemble mean of the three Julys for the experiment simulations.

4. Results

The comparison of the ensemble mean of the three control runs with the ensemble mean of the three experiment runs shows very little change in the surface fluxes of water vapor and sensible heat, but a large change in the atmospheric circulation and rainfall distribution. In the following seven subsections we shall find out why this is so.

a. Surface stress and boundary layer wind field

In this GCM, the vector surface stress, τ_s, is given by:

$$\tau_s = \rho_B C_D V_B V_B, \tag{1a}$$

$$C_D = C_U^2 = f(H_B, z_0, \mathrm{Ri}_B), \tag{1b}$$

$$\mathrm{Ri}_B = \frac{gH_B(\theta_{v,B} - \theta_{v,s})}{\theta \mathrm{U}_{v,s} V_B^2} \tag{1c}$$

where V_B is the vector wind in the lowest model layer, which is the dynamically driven and frictionally con-

trolled boundary layer; ρ_B is the air density; C_D is the surface drag coefficient; C_U is the bulk friction coefficient; z_0 is the surface roughness length; Ri_B is the bulk Richardson numbers; H_B is the boundary layer thickness, which equals the lowest model layer thickness in this GCM; $\theta_{v,b}$ is the virtual potential temperature in the middle of the lowest model layer; and $\theta_{v,s}$ is virtual potential temperature of the air at the surface.

The first three columns in Table 1 show, respectively, $\bar{V}_B$, $\overline{V_B^2}$ and $\bar{\tau}_s$; where the superior bar denotes the ensemble time mean. The calculations are shown, averaged over tropical and extratropical latitude zones, for land and ocean, separately.

We see that when the land surface roughness length is reduced from 45 cm in the control to 0.02 cm in the experiment, over the land the square of the boundary layer wind speed increased by about a factor of two and, at the same time, the surface stress decreased by about a factor of two.

By rearranging the terms in Eq. (1a) and taking the ensemble time mean, we obtain the mean density weighted surface drag coefficient, $\overline{\rho_B C_D}$; which is shown in the 4th column of the Table 1. As seen in the 5th column, over land $\overline{\rho_B C_D}$ decreased by about a factor of four from the control to the experiment; as one would expect with neutral thermal stability, when z_0 is reduced from 45 cm to 0.02 cm, with a boundary layer that is about 1 km deep.

Although no change was made in z_0 over the ocean, $\overline{V_B^2}$ for ocean regions increased by about 10%, while $\overline{\rho_B C_D}$ decreased by about 25% and $\bar{\tau}_s$ decreased by about 10%. The increase in $\overline{V_B^2}$ over the ocean was, presumably, an advection effect of the much larger increase of V_B^2 over land. That, by itself, as shown by Eq. (1b, 1c), would make the time and space averaged $\overline{\rho_B C_D}$ decrease by 10%. The rest of the decrease in $\overline{\rho_B C_D}$; may be due to a negative correlation between $(\theta_{v,B} - \theta_{v,s})$ and V_B because the time and space averaged $\overline{(\theta_{v,B} - \theta_{v,g})}$ hardly changes from the control to the experiment runs. The 10% decrease in $\bar{\tau}_s$ reflects the fact that $\overline{\rho_B C_D}$ decreases by more than $\overline{V_B^2}$ increases.

Figure 2 shows the ensemble mean of the boundary layer vector wind, V_B, for the three control runs (top panel), the three experiment runs (center panel), and the difference: experiment minus control (bottom panel), respectively. The velocity vectors have been rotated, but not stretched, to agree with the map projection, which is conformal at 39°N and S.

Figure 3 shows the ensemble mean of Ψ_B, the streamfunction of the boundary layer vector wind, V_B, as obtained from the solution of:

$$\nabla_\sigma^2 \Psi_B = \zeta_B, \tag{2}$$

and

$$\zeta_B = \mathbf{k} \cdot \nabla_\sigma \times V_B, \tag{3}$$

where ζ_B is the vertical component of the relative vorticity in the lowest model layer; and $\nabla_\sigma^2(\ )$ and $\nabla_\sigma \times (\ )$ are, respectively, the Laplacian and the curl operators on the σ surface.

Unlike the sea level pressure field, which over land shows the subterranean geostrophic wind, the streamfunction, Ψ_B, shows the nondivergent component of the wind in the atmospheric boundary layer above the surface. The largest changes in the nondivergent wind are over tropical South America, Africa, Arabia, India and Southeast Asia, and they correspond, to a large extent, with the change in the total vector wind, V_B, which can be seen in the bottom panel of Fig. 2. There is also a substantial change in the nondivergent component of the boundary layer wind over the extratropical oceans in the Southern Hemisphere. Past experience with GCM simulations has shown, however, that 90-day means are usually not long enough to average out the natural variability of the intense wave cyclones that move from west to east across the extratropical

TABLE 1. Analysis of the boundary-layer wind speed and surface stress for the ensemble mean.

Region	Boundary layer wind speed: $\bar{V}_B$ (m s^{-1})		Square of the boundary layer wind speed: $\overline{V_B^2}$ (m^2 s^{-2})		Magnitude of the surface stress: $\bar{\tau}_s$ (Pascals)		Density weighted surface drag coefficient $\overline{\rho_B C_D} = \bar{\tau}_s / \overline{V_B^2}$, (kg m^{-3} × 10^{-3})		Ratio: $\frac{(\overline{\rho_B C_D})_{\text{contr.}}}{(\overline{\rho_B C_D})_{\text{exp.}}}$
	Contr.	Exp.	Contr.	Exp.	Contr.	Exp.	Contr.	Exp.	
Extratropical land (20°–84°N, 20°S–84°S)	6.47	9.96	52.9	128.9	0.338	0.148	13.18	3.26	4.0
Tropical Land (20°N–20°S)	6.28	10.60	47.96	139.3	0.267	0.138	11.41	2.17	5.3
Extratropical Ocean (20°–84°N, 20°N–84°S)	9.41	9.87	116.9	128.1	0.147	0.134	3.05	2.31	1.3
Tropical Ocean (20°N–20°S)	8.32	8.64	84.76	90.6	0.106	0.097	3.01	2.41	1.2

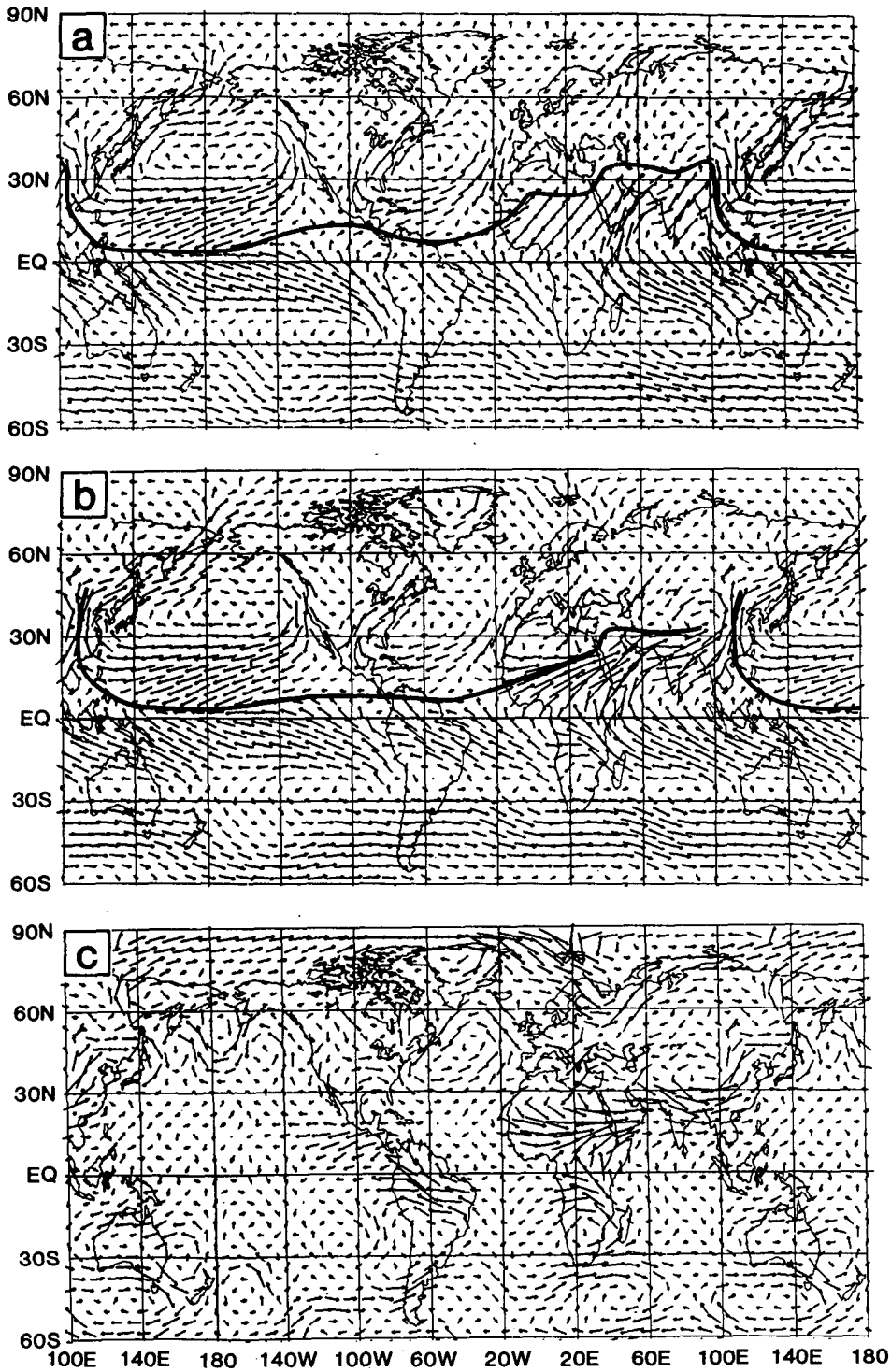

FIG. 2. Horizontal air velocity in the lowest model layer. Heavy line shows confluence of wind direction. Top: average of the three control runs (z_0 = 45 cm). Scale: 10° latitude = 10 m s^{-1}. Center: average of the three experiment runs (z_0 = 0.02 cm). Scale: 10° latitude = 10 m s^{-1}. Bottom: experiment minus control. Scale: 10° latitude = 5 m s^{-1}.

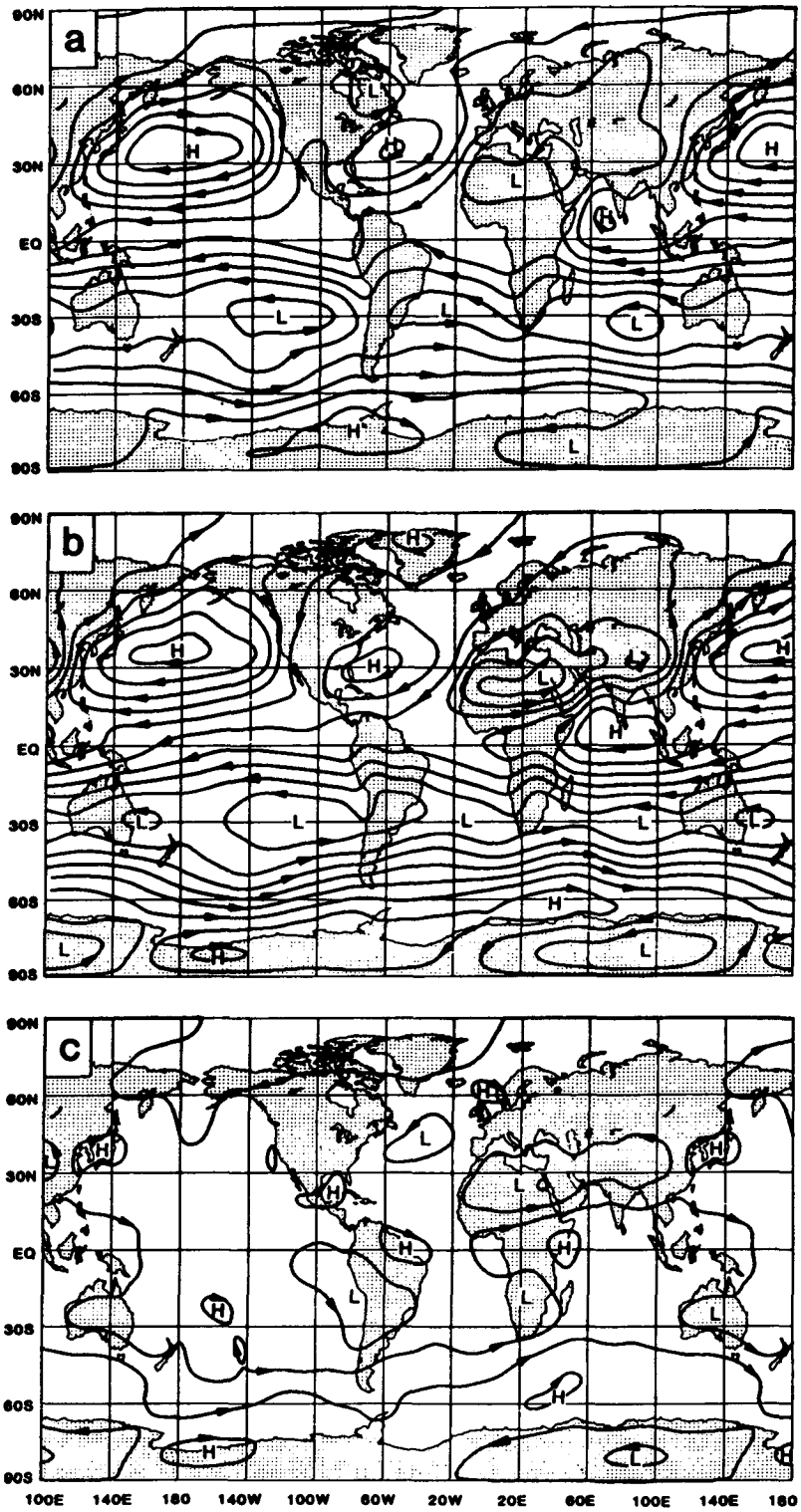

FIG. 3. Streamfunction of the horizontal air velocity in the lowest model layer. Contour interval = 5×10^6 m^2 s^{-1}. (Contour spacing of 500 km = 10 m s^{-1}.) Top: average of the three control runs. Center: average of the three experiment runs. Bottom: experiment minus control.

Southern Hemisphere oceans, especially in its winter season.

Figure 4 shows the ensemble mean of the horizontal mass convergence in the lowest model layer, $-\nabla_\sigma \cdot [V\Delta p/g]_B$, where $\Delta p_B = [(P_s - 10)/9]$ mb. Almost all of the changes in mass convergence that are larger than 2 gm m^{-2} s^{-1} (exceed about 20 mb day^{-1} equivalent pressure change) are found over the continents.

We have not analyzed the entire vorticity budget of the boundary layer, but Figure 4 shows the ensemble mean of one of its components, the curl of the surface stress divided by the Coriolis parameter $\mathbf{k} \cdot \nabla_\sigma \times \tau_s/f$, which produces horizontal mass convergence in the boundary layer. A comparison of the bottom panel of Fig. 5 with the bottom panel of Fig. 4 shows that the change in the curl of the surface stress accounts for most of the change in the boundary layer mass convergence.

b. *Water vapor transport convergence in the boundary layer*

Figure 6 shows the ensemble mean of the horizontal water vapor transport convergence in the boundary layer, $-\nabla_\sigma \cdot [Vq\Delta p/g]_B$. Over most of the land and some of the near coastal ocean, the change in the water vapor transport convergence is of the same order of magnitude as the convergence itself. Over the Central United States, there is a decrease in the water vapor transport convergence, with the maximum decrease exceeding 4 mm day^{-1}; over the east coast of the United States and adjacent west Atlantic Ocean there is an increase, with a maximum that exceeds 3 mm day^{-1}. Over midlatitude Eurasia, there are decreases and increases whose maxima exceed 2 to 3 mm day^{-1}. Over equatorial South America there are decreases of up to 5 mm day^{-1}; and there are increases up to about 5 mm day^{-1} over the adjacent equatorial oceans. Over the Western Sahara there is a decrease whose maximum is about 6 mm day^{-1}; and across the Sahel, and extending over the North Indian Ocean, there is an increase of up to 6 mm day^{-1}. Over equatorial East Africa, moisture convergence in the control changes to moisture divergence in the experiment, with a maximum change of about 6 mm day^{-1}. These are large changes, if we compare them with the global mean precipitation, which is of the order of 3 mm day^{-1}.

The close correspondence between the bottom panels of Figs. 4 and 6 shows that the change in the water vapor transport convergence in the boundary layer, $-\nabla_\sigma \cdot [Vq\Delta p/g]_B$, is produced mainly by the change in the mass convergence component, $-q_B\nabla_\sigma \cdot [V\Delta p/g]_B$, and not by a change in the water vapor advection component, $-V_B \cdot \nabla_\sigma [q\Delta p/g]_B$.

The horizontal water vapor transport convergence in model layer 8 (not presented here) is an order of magnitude smaller than that in the boundary layer. Therefore, the horizontal convergence of water vapor in strapped layer L is almost the same as in the boundary layer alone. As shown in Fig. 1, the convergence in strapped layer L is a source of water vapor for the shallow and the deep convective clouds.

c. *Surface evaporation and sensible heat flux*

In this GCM, the land surface evaporation, E, is given by:

$$E = \beta E^*, \tag{4}$$

$$\beta = 1 - e^{-6.8(W/W^*)}, \tag{5}$$

$$E^* = \rho_B C_U C_H V_B [q^*(T_g^*) - q_B], \tag{6}$$

where E^* is the potential evapotranspiration; $q^*(T_g^*)$ is the saturation specific humidity at the moist lysimeter temperature, T_g^*; q_B is the actual boundary layer specific humidity; W/W^* is the soil wetness; C_U is the bulk aerodynamic friction coefficient; and C_H is the bulk aerodynamic transport coefficient for water vapor and heat. As was stated before, W/W^* is climatologically prescribed and, therefore, β, as given by Eq. (5), is the same in the control and the experiment runs.

It might appear, from equations (6) and (4), that when $(C_U C_H)$ is reduced by a factor of 4, there would be some substantial decrease in E^* and E. But examination of Fig. 7 shows that there is almost no change in the surface evaporation.

Similarly, the sensible heat transfer from the ground to the air is given by:

$$H = \rho_B C_U C_H V_B (T_g - T_a), \tag{7}$$

where T_g is the ground temperature and T_a is the surface air temperature.

From Eq. (7), it might be inferred that a 4-fold decrease in $(C_U C_H)$ would produce a substantial decrease in H. But examination of Fig. 8 shows that there is almost no change in the surface sensible heat flux.

The fact that neither the evaporation nor the sensible heat flux change follows from the constraints on the surface energy balance in the GCM calculations.

When averaged over a month or more, the heat storage in the ground is small and the equation of surface energy balance over land reduces to:

$$\lambda E + H = R_n, \tag{8}$$

where R_n is the net radiation flux at the surface and λ is the latent heat of evaporation. The shortwave component of R_n depends on the surface albedo and the cloud cover. The surface albedo is climatologically prescribed and is the same in the control and experiment runs. As stated before, in this GCM only the large scale condensation clouds interact with the radiation fluxes; the simulation produces very few large scale clouds over the continents in the summer months.

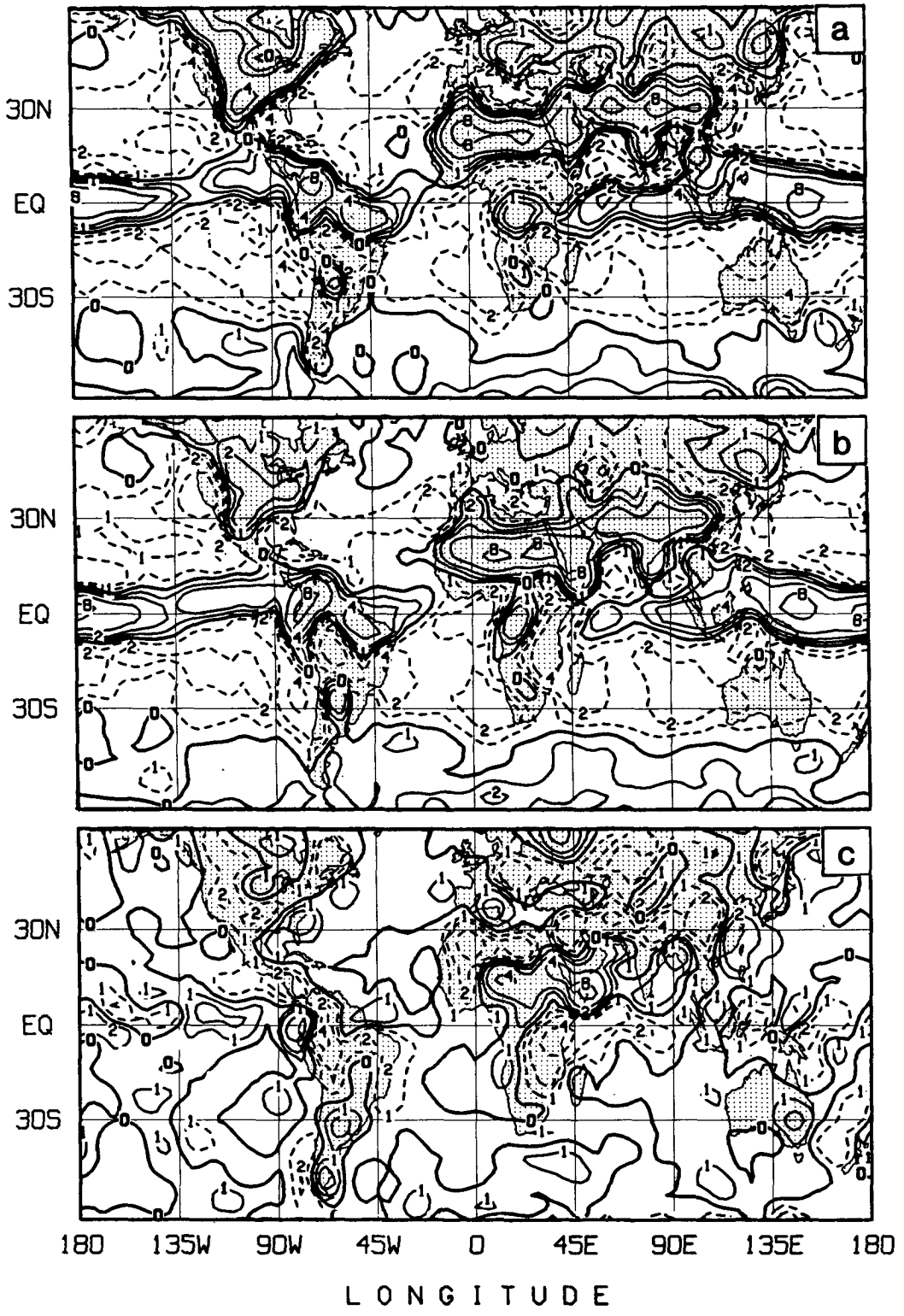

FIG. 4. Horizontal mass convergence in the lowest model layer. Contours for ±0, 1, 2, 4, 8, 12, 16 . . . gm m^{-2} s^{-1}. Dashed lines show negative values. Top: average of the three control runs. Center: average of the three experiment runs. Bottom: experiment minus control.

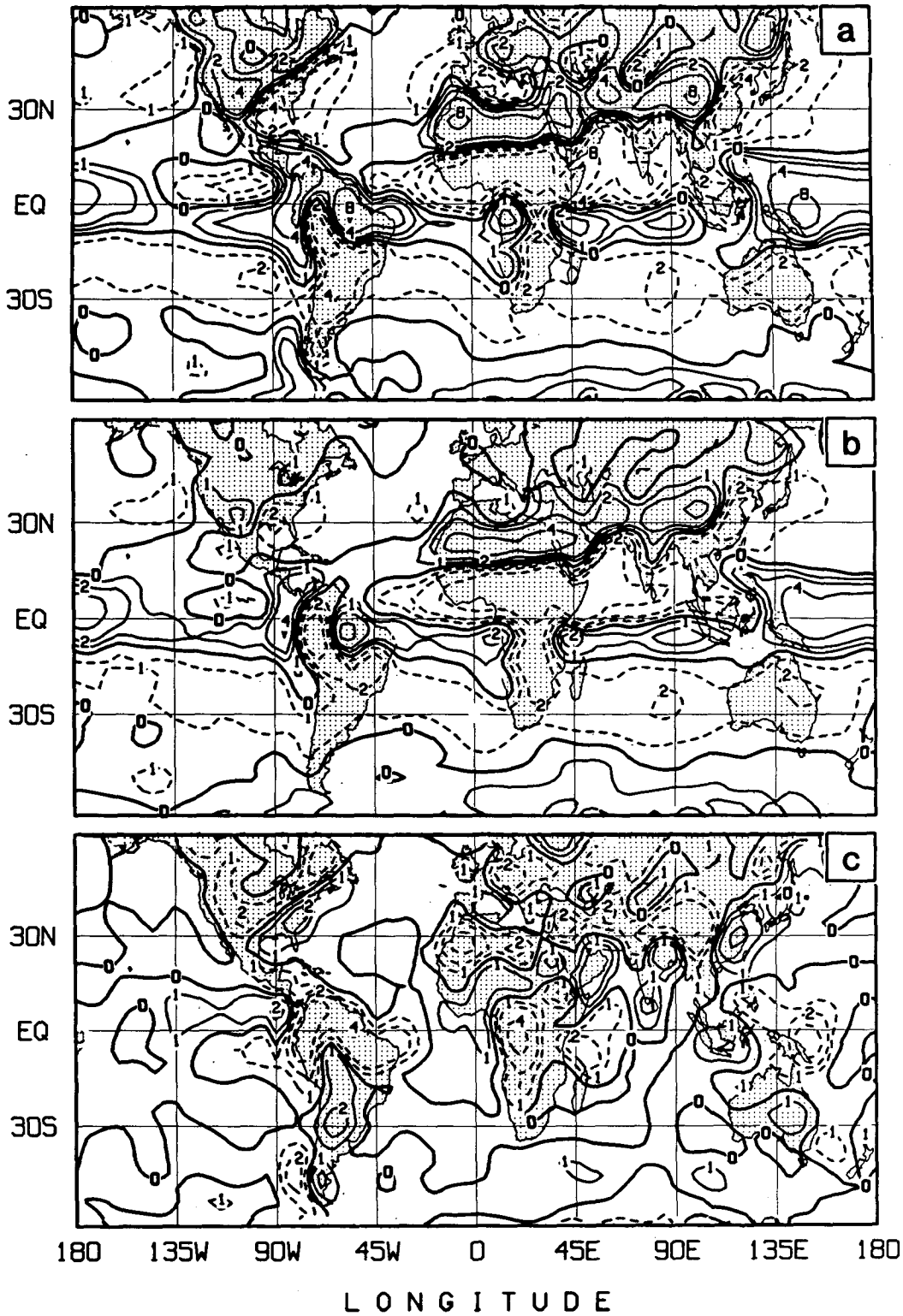

FIG. 5. Curl of the surface stress, divided by the Coriolis parameter. Contours for ±0, 1, 2, 4, 8, 12, 16 . . . gm m^{-2} s^{-1}. Dashed lines show negative values. Top: average of the three control runs. Center: average of the three experiment runs. Bottom: experiment minus control.

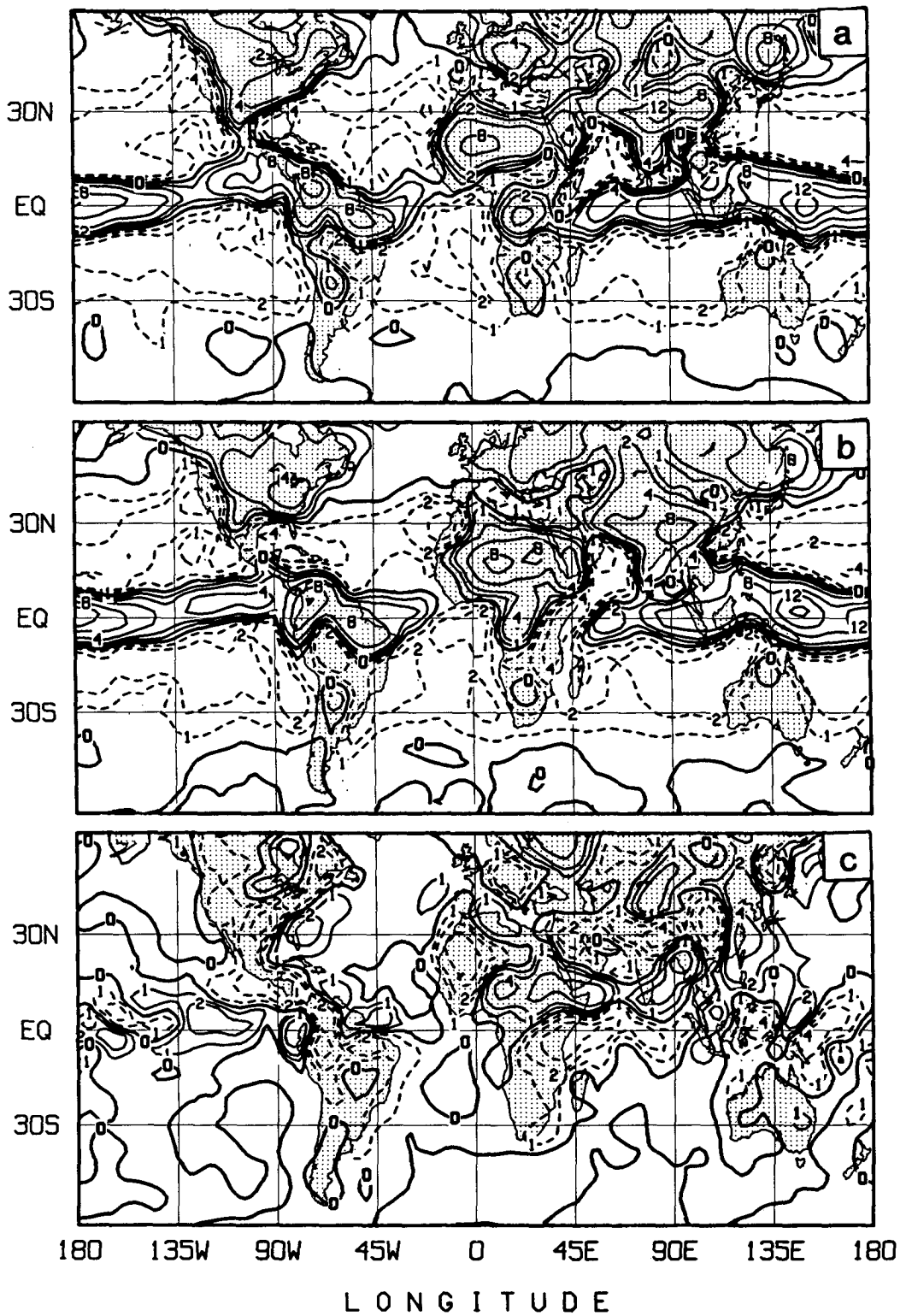

FIG. 6. Convergence of the horizontal water vapor transport in the lowest model layer. Contours for ±0, 1, 2, 4, 8, 12, 16 . . . mm day^{-1}. Dashed lines show negative values. Top: average of the three control runs. Center: average of the three experiment runs. Bottom: experiment minus control.

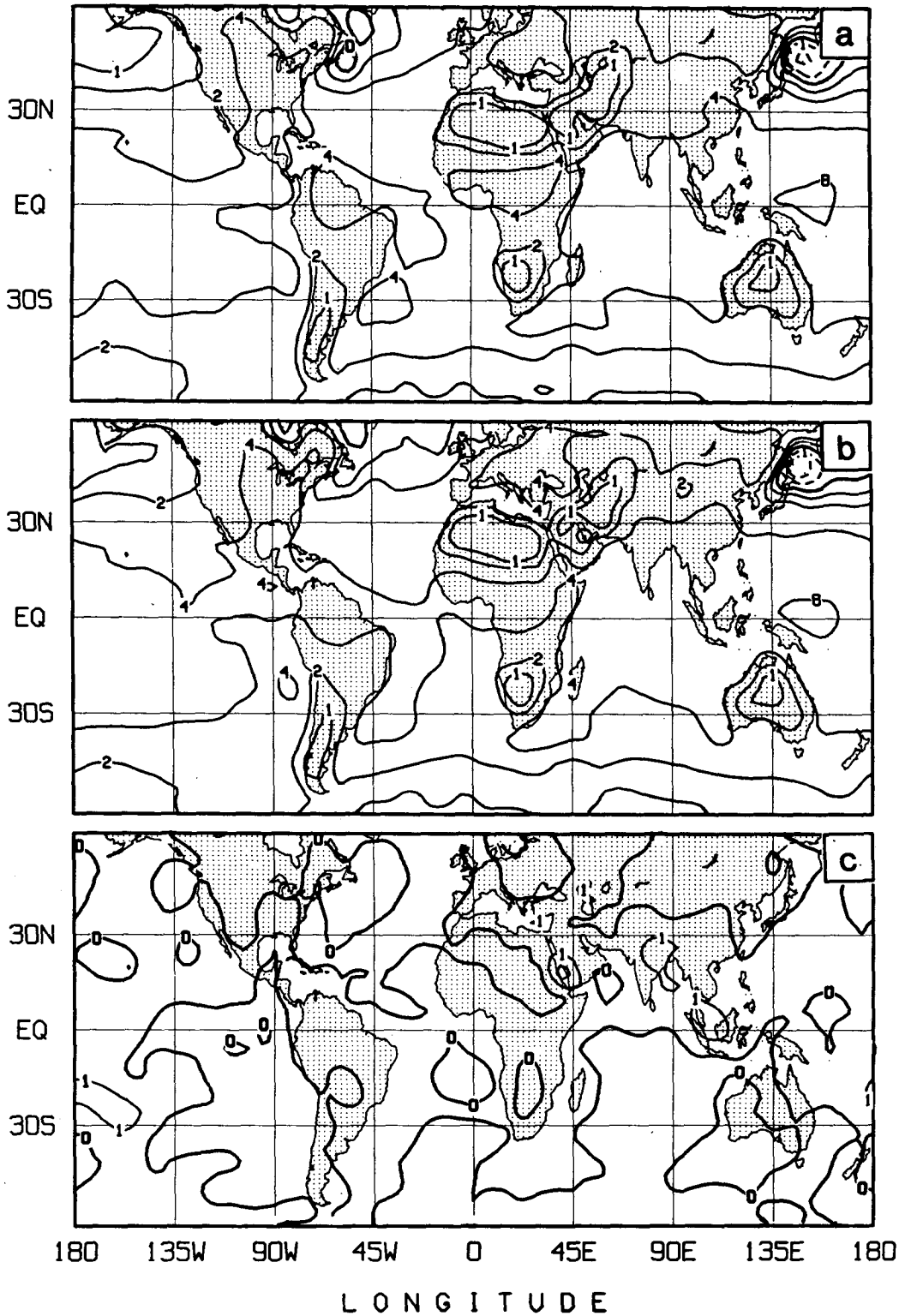

FIG. 7. Surface evaporation. Contours for ±0, 1, 2, 4, 8, 12, 16 . . . mm day^{-1}. Dashed lines show negative values. Top: average of the three control runs. Center: average of the three experiment runs. Bottom: experiment minus control.

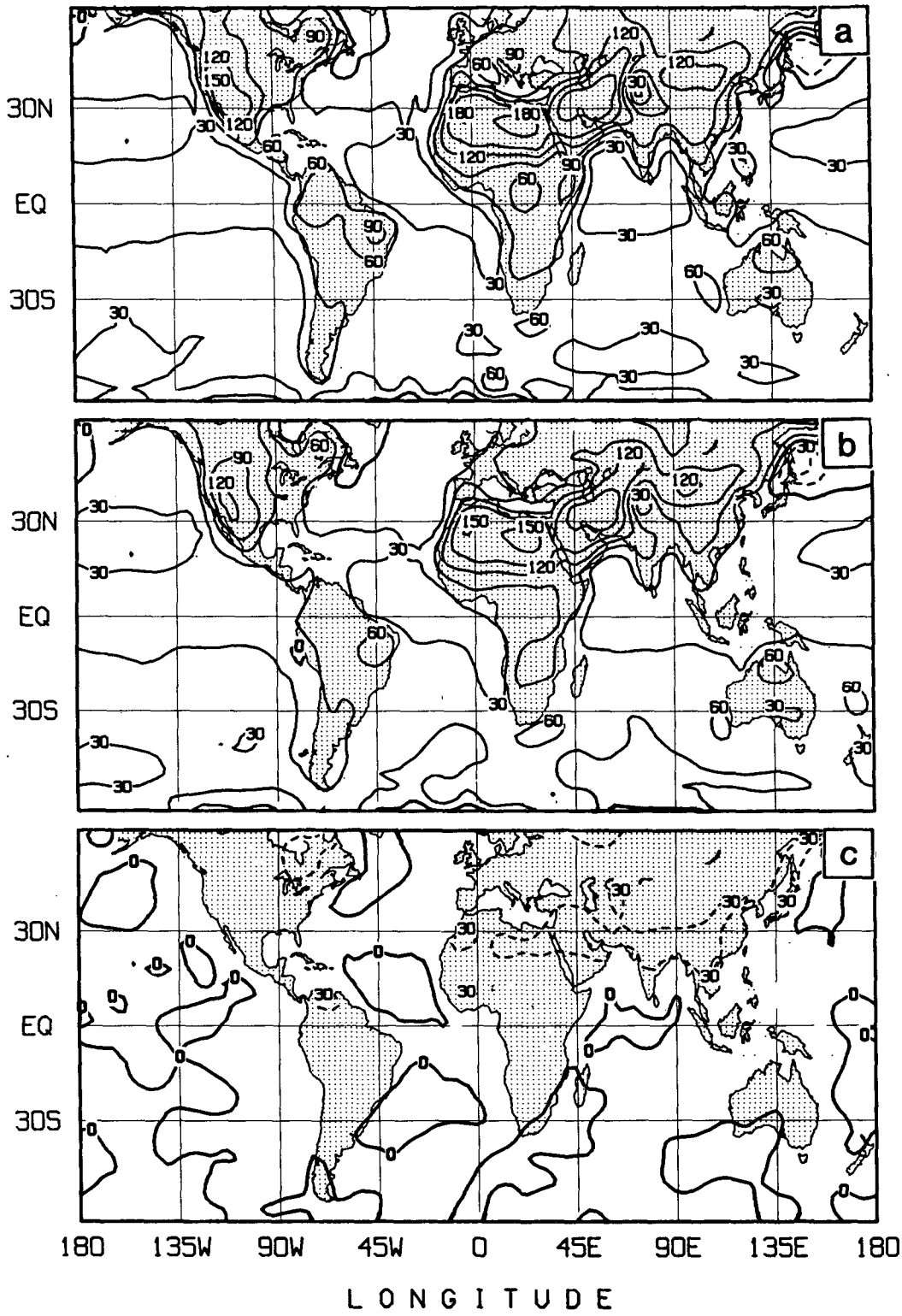

FIG. 8. Surface sensible heat flux, watt m^{-2}. Dashed lines show negative values. Top: average of the three control runs. Center: average of the three experiment runs. Bottom: experiment minus control.

Consequently, there is very little change in the shortwave component of R_n, over land.

The longwave component of R_n, in the GCM, depends on the ground and air temperatures and on the large scale cloudiness. But the temperatures do not change much from control to experiment and, as indicated before, the simulation produces very few large scale clouds over land in the summer season. Thus, the net surface radiation flux, R_n, is almost the same in the control and experiment, and $\lambda E + H$ must be almost the same.

What can and do change are the humidity and temperature differences: $[q^*(T_g^*) - q_B]$ and $(T_g - T_a)$. For example, in the Sahara, at 26°N, 15°E, where W/W^* is very small, and where there is only a small change in V_B, $(\bar{T}_g - \bar{T}_a) = (42.4 - 39.3) = 3.3$°C in the control and $(47.5 - 34.5) = 13.0$°C in the experiment. This is a 4-fold increase in $(\bar{T}_g - \bar{T}_a)$, which compensates the 4-fold decrease in $(C_U C_H)$.

d. *Water budget of the lowest strapped layer*

Figure 9 shows the ensemble mean of the surface evaporation plus the convergence of the horizontal water vapor transport in strapped-layer L. Except for a small amount of water vapor removal by the large scale precipitation, which is produced by supersaturation of the air in layer L, the rest of the water vapor must be removed by a vertical transfer through the top of layer L. In this GCM the transfer processes across the top of layer L are the upward fluxes of water vapor by deep precipitating and/or shallow nonprecipitating cumulus clouds, shown by the double stroked arrows in Figure 1 and the upward or downward advection of water vapor in the clear areas that surround the cloud towers. Because there is almost no change in the surface evaporation and the water vapor transport convergence in layer 8 is small, the bottom panel of Fig. 9 is very much like the bottom panel of Fig. 6.

e. *Convective precipitation*

Figure 10 shows the ensemble mean convective precipitation. A striking but spurious feature, in both the control and the experiment, is the large amount of precipitation over all of the Sahara region. As one can see by comparing the top and center panels of Figs. 6, 7 and 10, it is the transport convergence in the boundary layer which supplies the water vapor for this unrealistic convective precipitation over the Sahara.

In nature, there is indeed a boundary layer water vapor transport convergence over the Sahara; however, Water vapor is transferred to the middle and upper troposphere by dry convection in the deep layer of unstable air that forms during the middle of the day over the hot desert surface, with the water vapor being removed from the middle and upper troposphere by horizontal advection. In our GCM, however, dry convection does not transfer water vapor upward. Consequently, the water vapor which converges in the boundary layer over the Sahara accumulates in strapped layer L until $h_L > (h_M^*, h_U^*)$, and then deep, precipitating cumulus convection removes the water vapor from layer L. In a subsequent version of this GCM a vertical transfer of water vapor by dry convection was added and that stopped the convective precipitation over the Sahara. (See Sud and Molod 1988, for further details.)

What is relevant to the present study is the change in the convective precipitation from control to experiment, which is shown in the bottom panel of Fig. 10. We see that most of the change in the convective precipitation corresponds with the change in the boundary layer water vapor transport convergence, shown in the bottom panel of Fig. 6.

f. *Total precipitation*

Figure 11 shows the ensemble mean of the total precipitation, which is the sum of the convective and the large scale precipitation. Over the land the total precipitation is mainly convective in both the control and experiment runs. Therefore, the change in the total precipitation is almost the same as the change in the convective precipitation.

Most of the large scale precipitation is over the ocean. In the Southern Hemisphere west wind zone, 30°–60°S, the large scale precipitation and the convective precipitation are of about equal magnitude, each having ensemble mean maxima of about 2.5 mm day^{-1}. Over the tropical Indian Ocean and westernmost equatorial Pacific Ocean, where almost all of the precipitation is convective, there are changes of the order of ±2 mm day^{-1}.

g. *Statistical significance*

The bottom panel of Fig. 11 shows the difference of the ensemble mean total precipitation between the control and experiment runs. The three panels of Fig. 12 show the differences for each of the three separate pairs of July runs. We see that over land the changes in the individual years resemble the ensemble mean change. Over the ocean, however (except for the tropical Indian Ocean), the changes are different in different years and cancel out in the ensemble mean.

The statistical significance of the difference in the total precipitation is shown in Fig. 13, which is a map of $t(\bar{P})$ calculated by:

$$t(\bar{P}) = (\bar{P}_{\text{exp.}} - \bar{P}_{\text{contr.}})\left[\frac{N}{\sigma(P)^2_{\text{exp.}} + \sigma(P)^2_{\text{contr.}}}\right]^{0.5}, \quad (9)$$

where P is the precipitation in the individual month, N (=3) is the number of pairs of months, $\sigma(P)$ is the variance of P, and the superior bar denotes the ensem-

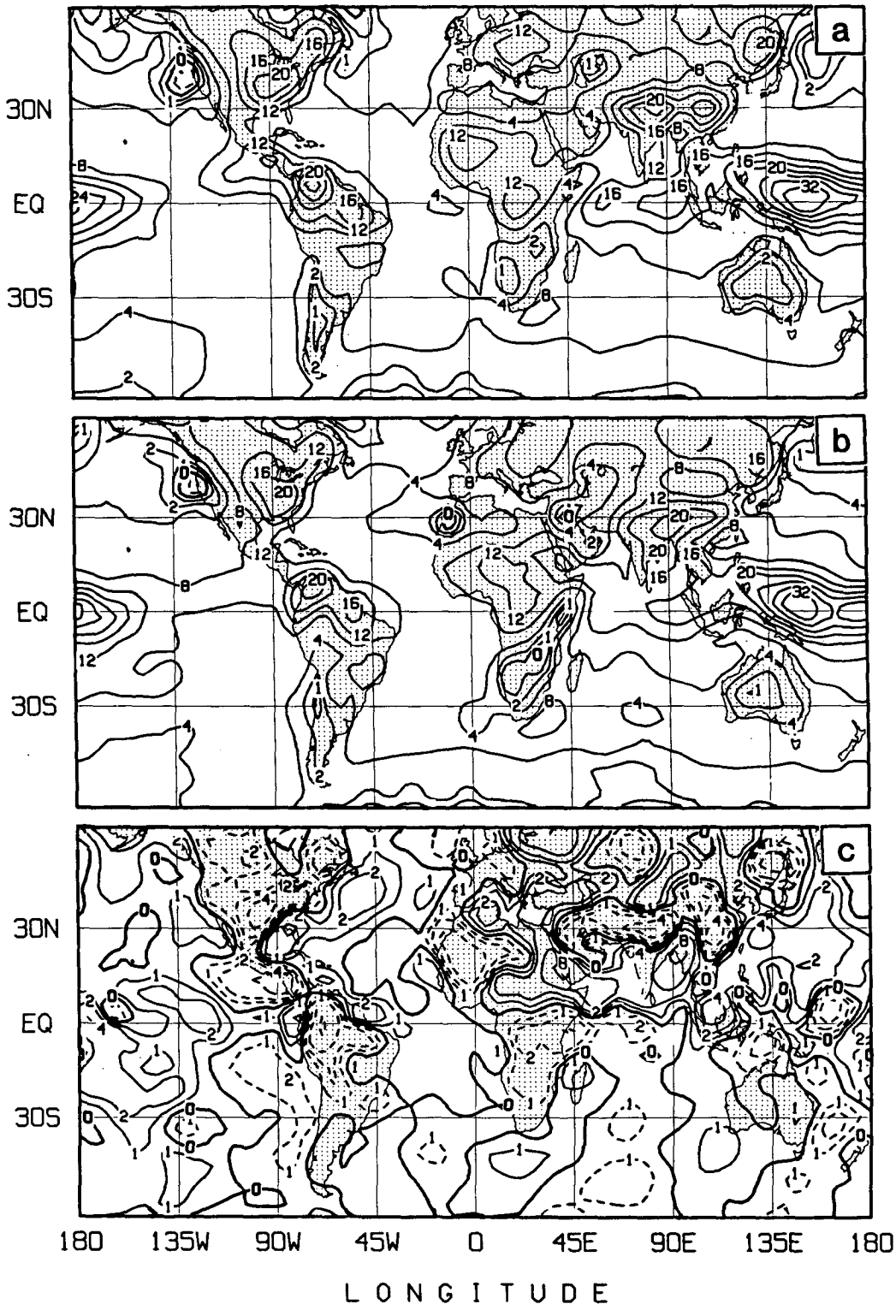

FIG. 9. Surface evaporation plus convergence of the horizontal water vapor transport in strapped-layer L. Contours for ±0, 1, 2, 4, 8, 12, 16 . . . mm day^{-1}. Dashed lines show negative values. Top: average of the three control runs. Center: average of the three experiment runs. Bottom: experiment minus control.

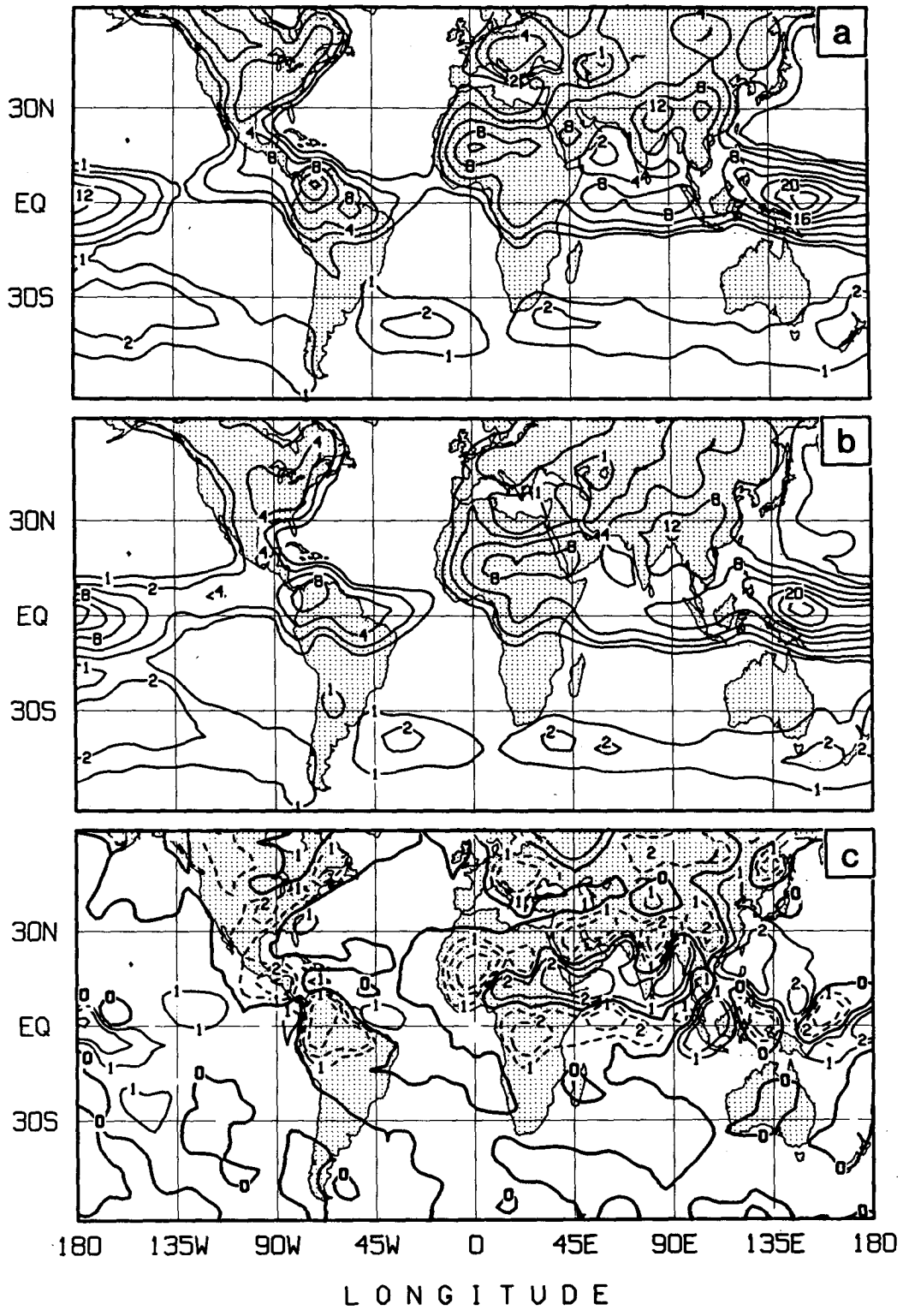

FIG. 10. Convective precipitation. Contours for ±0, 1, 2, 4, 8, 12, 16 . . . mm day^{-1}. Dashed lines show negative values. Top: average of the three control runs. Center: average of the three experiment runs. Bottom: experiment minus control.

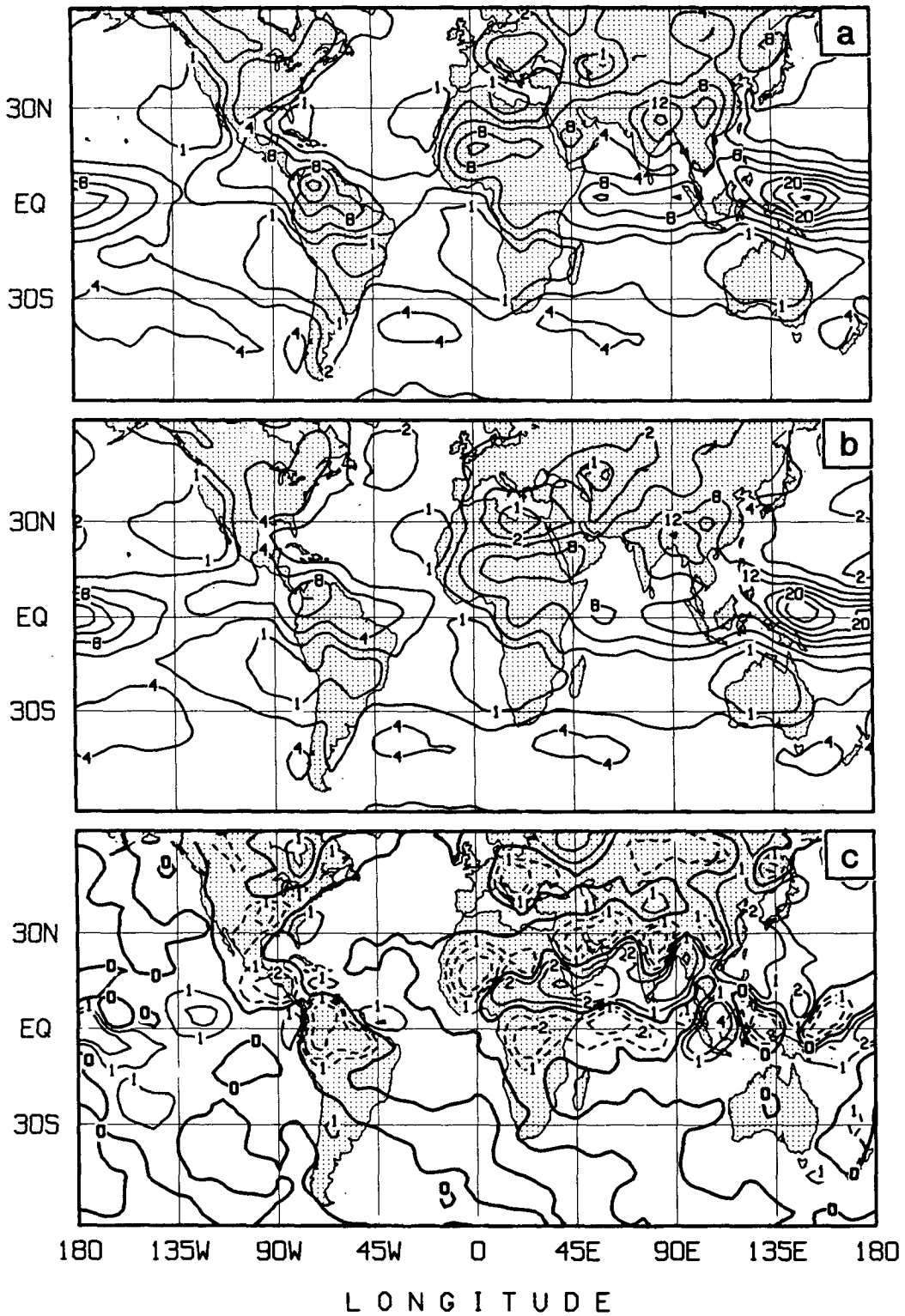

FIG. 11. Total precipitation. Contours for ±0, 1, 2, 4, 8, 12, 16 . . . mm day^{-1}. Dashed lines show negative values. Top: average of the three control runs. Center: average of the three experiment runs. Bottom: experiment minus control.

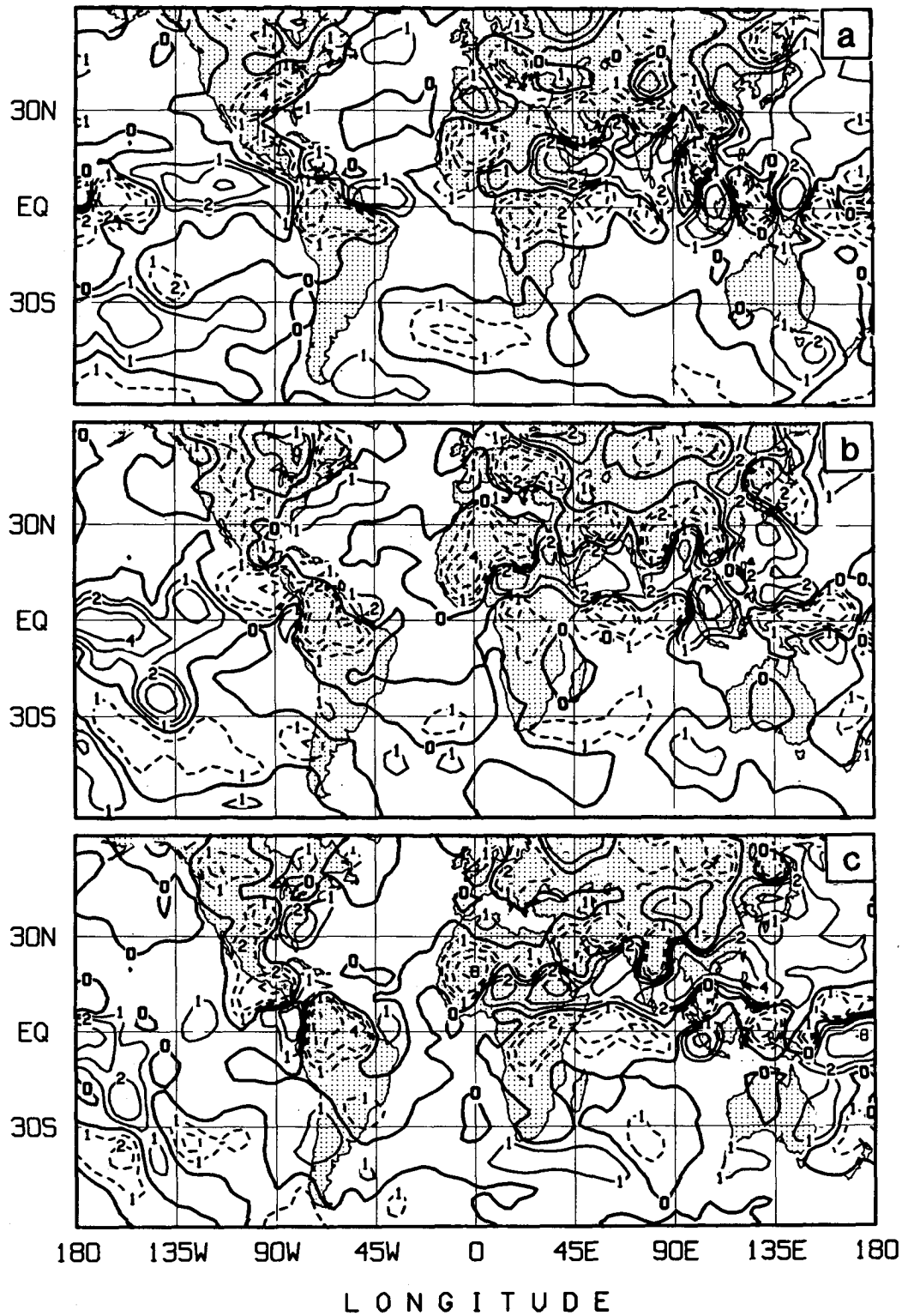

FIG. 12. Difference of the total rainfall (experiment minus control) in each of the three separate pairs of July runs. Contours for ±0, 1, 2, 4, 8, 12, 16 . . . mm day^{-1}. Dashed lines show negative values.

ble mean. The shaded areas on the map highlight the regions where $t(\bar{P})$ is greater than ±2.8.

When we compare the bottom panel of Fig. 11 with Fig. 13, we see that most of the land regions which have a large difference in the ensemble mean precipitation also have a $t(\bar{P})$ value greater than ±2.8. In these regions, therefore, there is only a 5% chance that the change in the precipitation could have occurred without the change in z_0.

5. Summary and discussion

In this GCM sensitivity study, a reduction of the prescribed land surface roughness length from 45 cm to 0.02 cm, which corresponds to about a four-fold reduction in the bulk aerodynamic surface drag coefficient, caused a significant change in the rainfall distribution over the land and adjacent regions of the oceans. This was produced mainly by the change in the boundary layer water vapor transport convergence.

The reduction of the surface roughness produced almost no change in the surface evaporation and surface sensible heat flux. This is understandable because the control and the experiment runs used the same climatologically prescribed fields of surface albedo and soil wetness because no interactions were allowed between the convective clouds and the radiation fluxes.

The question arises as to how the precipitation might be affected if we used a GCM in which the soil moisture and a vegetation dependent land surface albedo interact with the precipitation and the radiation fluxes interact with the convective clouds. In such a model, soil moisture would increase (decrease) with the increased (decreased) precipitation; and the surface albedo would decrease (increase) with the increased (decreased) soil moisture, as a consequence of increased (decreased) vegetation. Both of these will produce positive feedbacks on the precipitation. (See, for example, the soil moisture and albedo sensitivity experiments reviewed by Mintz 1984, and by Rowntree 1985). We expect, therefore, that interactive soil moisture and interactive surface albedo will produce even larger changes in the precipitation than what has been found in this study. On the other hand, interaction between the convective clouds and the radiation fluxes may produce positive or negative feedbacks on the convective precipitation. The net effect of all of these feedbacks working together, when the surface roughness is changed, remains to be determined.

As shown by Sud and Molod (1988), a GCM in which dry convection transfers water vapor from the boundary layer to the free atmosphere does not produce precipitation over the Sahara desert. In such a model, the influence of the surface roughness on the precipi-

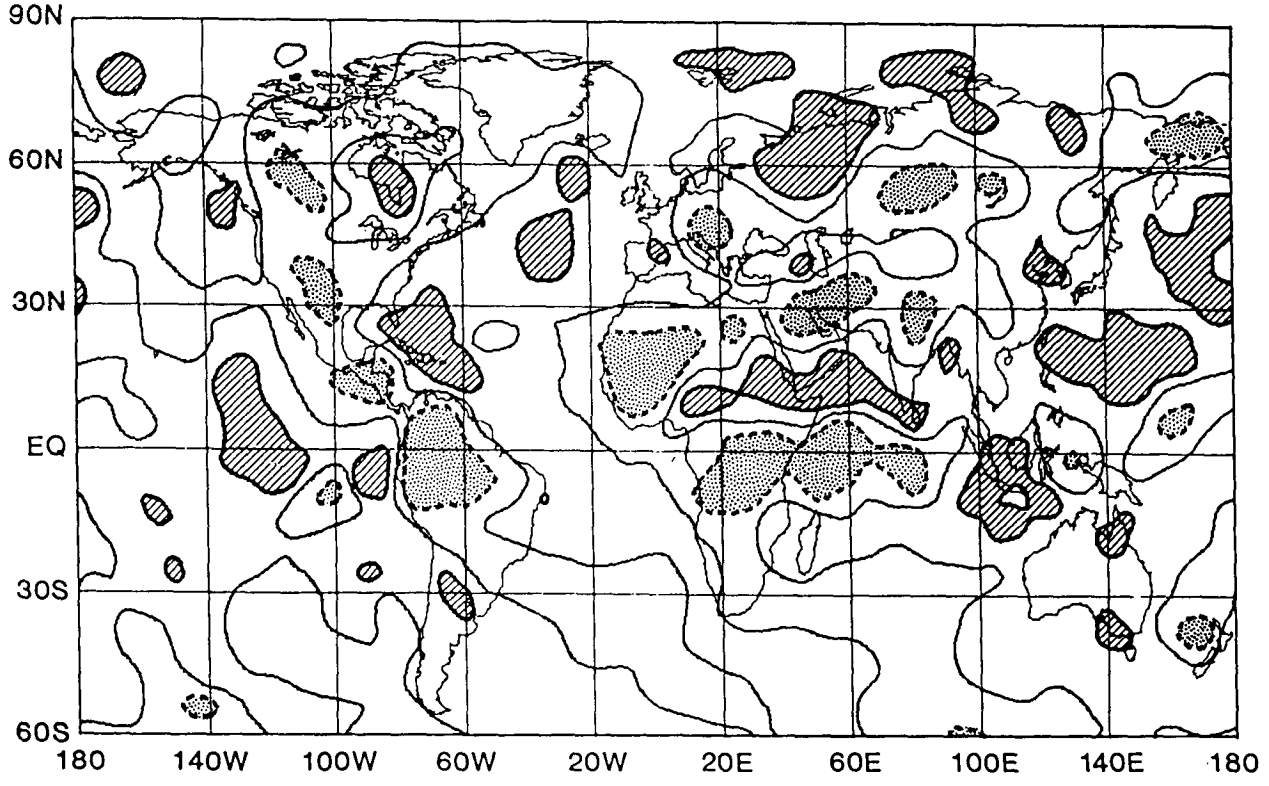

FIG. 13. Student's t-test analysis of the rainfall differences between the control and experiment runs; t greater than ±2.8 represents over 95% significance. The dotted and ruled shaded areas show the regions of 95% confidence for dry and wet conditions.

tation over the Sahara will be largely eliminated. But in the desert margin regions, such as the Sahel, and over other evaporating land where dry convection is not very intense and deep, we expect the results to be about the same as in this study.

Many studies have shown that vegetation influences the atmospheric circulation and precipitation because vegetation affects the surface albedo and evapotranspiration. This study focuses on the third effect of vegetation, its contribution to the land surface roughness. We have shown that the surface roughness significantly influences the atmospheric circulation and precipitation, especially in the tropics, because it directly affects the boundary layer water vapor transport convergence.

Acknowledgments. The authors thank the anonymous reviewers of this paper for recommending the analysis shown in Table 1. They thank William E. Smith and Gregory K. Walker for their help in making the computer runs, the diagnostic calculations and the computer graphics; Laura Rumburg for drafting the figures; and Quy Philpot for typing the manuscript.

For this research, Dr. Y. C. Sud was supported by NASA RTOP: 677-21-37. The participation of Professors Y. Mintz and J. Shukla was supported by grants to the University of Maryland from the National Science Foundation (Grants ATM-8309767 and ATM-0153818) and from the National Aeronautics and Space Administration (Grant NAG5-383).

REFERENCES

Arakawa, A., 1969: Parameterization of cumulus convection. Appendix I, Numerical Simulaton of the General Circulation of the Atmosphere, A. Arakawa, A. Katayama and Y. Mintz. *Proceedings of the WMO/IUGG Symposium on Numerical Weather Prediction, Tokyo 1968.* pp. IV-7 to IV-8-12.

——, 1972: Design of the UCLA general circulation model, for the numerical simulation of weather and climate. Tech. Rep. 7, Dept. Meteorol., University of California, Los Angeles, 35–77.

Baumgartner, A., H. Mayer and W. Metz, 1977: Weltweite verteilund des rauhigkeitsparameters z_0 mit anwendung auf die energiedissipation an der erdoberflache. *Meteorol. Resch.*, **30,** 43–48.

Charney, J. G., W. J. Quirk, S. H. Chow and J. Kornfield, 1977: A comparative study of the effects of albedo change on drought in semi-arid regions. *J. Atmos. Sci.*, **34,** 1366–1385.

Crutcher, H. L., and D. M. Davis, 1969: *U.S. Navy Marine Climatic Atlas of the World.* Vol. VIII, The World. NAVAIR 50-1C-54, Naval Weather Service Command, Washington, DC.

Deardorff, J. W., 1972: Parameterization of the planetary boundary layer for use in general circulation models. *Mon. Wea. Rev.*, **100,** 83–106.

Fiedler, F., and H. A. Panofsky, 1971: The geostrophic drag coefficient over heterogeneous terrain. Paper presented at the *Second Canadian Conference on Micrometerology,* MacDonald College, Quebec, 10–12 May 1971.

——, and ——, 1972: The geostrophic drag coefficient and the "effective" roughness length. *Quart. J. Roy. Met. Soc.*, **98,** 213–220.

Kalnay, E., R. Balgovind, W. Chao, D. Edelmann, J. Pfaendtner, L. Takacs and K. Takano, 1983: Documentation of the GLAS Fourth Order General Circulation Model. *NASA Tech. Memo. 86064,* Vol. 1, NTIS.

Manabe, S., 1975: A study of the interaction between the hydrological cycle and climate using a mathematical model of the atmosphere. *Proceedings of Conference on Weather and Food,* MIT, Cambridge, Mass., 9–11 May 1975, p. 21–45.

Mintz, Y., 1984: The sensitivity of numerically simulated climates to land surface boundary conditions. Chapter 6, in *The Global Climate.* (J. T. Houghton, Ed.) Cambridge University Press, Cambridge/London/New York, p. 79–105.

——, and Y. Serafini, 1984: Global fields of normal monthly soil moisture, as derived from observed precipitation and an estimated potential evapotranspiration. Part V, *Final Scientific Report Under NASA Grant No. NAS5-26.* Dept. Meteorology, Univ. of Maryland, College Park, Md 20742.

Posey, J. W., and P. F. Clapp, 1964: Global distribution of normal surface albedo. *Geophysical International,* **4(1),** 33–48.

Randall, D. A., 1982: Monthly and seasonal simulations with the GLAS climate model. *Proceedings of the Workshop on Intercomparison of Large-Scale Models Used for Extended Range Forecasts,* European Centre for Medium Range Weather Forecasts, Reading, England. 30 June–2 July, 1982. p. 107–166.

Rowntree, P. R., 1985: Review of general circulation models as a basic for predicting the effects of vegetation change on climate. *Proceedings of the United Nations Univerity Workshop on Forests, Climate and Hydrology,* Oxford, 26–30 March 1984.

Shukla, J., and Y. Mintz, 1982: Influence of land surface evapotranspiration on the Earth's climate. *Science,* **215,** 1498–1501.

——, D. Straus, D. A. Randall, Y. Sud and L. Marx, 1982: Winter and summer simulations with the GLAS climate model. *NASA Tech. Memo. 83866,* 282 pp.

Somerville, R. C. J., P. Stone, M. Halem, E. Hansen, J. S. Hogan, L. M. Druyan, G. Russell, A. A. Lacis, W. J. Quirk and J. Tenenbaum, 1974: The GISS model of the global atmosphere. *Jour. Atmo. Sci.*, **31,** 84–117.

Sud, Y. C., and M. J. Fennessy, 1982: A study of the influence of surface albedo on July Circulation in semi-arid regions using the GLAS GCM. *J. Climatol.*, **2,** 105–125.

——, and W. E. Smith, 1984: Ensemble formulation of surface fluxes and improvement in evapotranspiration and cloud parameterization in a GCM. *Bound. Layer Meteor.*, **33,** 1–35.

——, and ——, 1985a: The influence of surface roughness of deserts on July circulation—a numerical study. *Bound. Layer Meteor.*, **33,** 1–35.

——, and ——, 1985b: Influence of local land surface processes on the Indian Monsoon: A numerical study. *Jour. Climate and Appl. Meteor.*, **24,** 1015–36.

——, and A. Molod, 1988: The roles of dry convection, cloud-radiation feedback processes and the influence of recent improvements in the parameterization of convection in the GLA GCM. *Mon. Wea. Rev.*, **116,** 2366–2387.

Walker, J., and P. R. Rowntree, 1977: The effect of soil moisture on circulation and rainfall in a tropical model. *Quart. J. Roy. Meteor. Soc.*, **103,** 29–46.